TU/e EINDHOVEN UNIVERSITY OF TECHNOLOGY

Three-dimensional histopathological reconstruction as a reliable ground truth for prostate cancer studies

Citation for published version (APA):
Wildeboer, R. R., Schalk, S. G., Demi, L., Wijkstra, H., & Mischi, M. (2017). Three-dimensional histopathological reconstruction as a reliable ground truth for prostate cancer studies. *Biomedical Physics & Engineering Express*, *3*(3), Article 35014. https://doi.org/10.1088/2057-1976/aa7073

Document license:
TAVERNE

DOI:
10.1088/2057-1976/aa7073

Document status and date:
Published: 01/06/2017

Document Version:
Publisher's PDF, also known as Version of Record (includes final page, issue and volume numbers)

Please check the document version of this publication:

• A submitted manuscript is the version of the article upon submission and before peer-review. There can be important differences between the submitted version and the official published version of record. People interested in the research are advised to contact the author for the final version of the publication, or visit the DOI to the publisher's website.
• The final author version and the galley proof are versions of the publication after peer review.
• The final published version features the final layout of the paper including the volume, issue and page numbers.

Link to publication

General rights
Copyright and moral rights for the publications made accessible in the public portal are retained by the authors and/or other copyright owners and it is a condition of accessing publications that users recognise and abide by the legal requirements associated with these rights.

• Users may download and print one copy of any publication from the public portal for the purpose of private study or research.
• You may not further distribute the material or use it for any profit-making activity or commercial gain
• You may freely distribute the URL identifying the publication in the public portal.

If the publication is distributed under the terms of Article 25fa of the Dutch Copyright Act, indicated by the "Taverne" license above, please follow below link for the End User Agreement:

www.tue.nl/taverne

Take down policy
If you believe that this document breaches copyright please contact us at:

openaccess@tue.nl

providing details and we will investigate your claim.

Download date: 07. Nov. 2026

IOPscience iopscience.iop.org

Home Search Collections Journals About Contact us My IOPscience

Three-dimensional histopathological reconstruction as a reliable ground truth for prostate cancer studies

This content has been downloaded from IOPscience. Please scroll down to see the full text.

2017 Biomed. Phys. Eng. Express 3 035014

(http://iopscience.iop.org/2057-1976/3/3/035014)

View the table of contents for this issue, or go to the journal homepage for more

Download details:

IP Address: 131.155.151.22
This content was downloaded on 04/07/2017 at 10:42

Please note that terms and conditions apply.

You may also be interested in:

Contouring variability of human- and deformable-generated contours in radiotherapy for prostate cancer
Stephen J Gardner, Ning Wen, Jinkoo Kim et al.

MR elastography to measure the effects of cancer and pathology fixation on prostate biomechanics, and comparison with T1, T2 and ADC
Deirdre M McGrath, Jenny Lee, Warren D Foltz et al.

Computer-aided diagnosis of prostate cancer in the peripheral zone using multiparametric MRI
Emilie Niaf, Olivier Rouvière, Florence Mège-Lechevallier et al.

Texture features on T2-weighted magnetic resonance imaging: new potential biomarkers for prostate cancer aggressiveness
A Vignati, S Mazzetti, V Giannini et al.

Automatic computer-aided detection of prostate cancer based on multiparametric magnetic resonance image analysis
P C Vos, J O Barentsz, N Karssemeijer et al.

A feasibility study to investigate the use of thin-plate splines to account for prostate deformation
Niranjan Venugopal, Boyd McCurdy, Alex Hnatov et al.

Registration of CT to pre-treatment MRI for planning of MR-HIFU ablation treatment of painful bone metastases
Yolanda H Noorda, Lambertus W Bartels, Merel Huisman et al.

Biomedical Physics & Engineering Express

PAPER

Three-dimensional histopathological reconstruction as a reliable ground truth for prostate cancer studies

R R Wildeboer[1], S G Schalk[1,2], L Demi[1], H Wijkstra[1,2] and M Mischi[1]

[1] Department of Electrical Engineering, Eindhoven University of Technology, De Zaale, 5600 MB Eindhoven, The Netherlands
[2] Department of Urology, Academic Medical Center, Meibergdreef 9, 1105 AZ Amsterdam, The Netherlands

E-mail: r.r.wildeboer@tue.nl

RECEIVED
25 January 2017

REVISED
21 April 2017

ACCEPTED FOR PUBLICATION
2 May 2017

PUBLISHED
18 May 2017

Keywords: histopathology, prostate cancer, radical prostatectomy, tumour interpolation, validation

Abstract

To validate new imaging modalities for prostate cancer, images must be three-dimensionally correlated with the histological ground truth. In this work, an interpolation algorithm is described to construct a reliable three-dimensional reference from two-dimensional (2D) histological slices. Eight clinically relevant *in silico* phantoms were designed to represent difficult-to-reconstruct tumour structures. These phantoms were subjected to different slicing procedures. Additionally, controlled errors were added to investigate the impact of varying slicing distance, front-face orientation, and inter-slice misalignment on the reconstruction performance. Using a radial-basis-function interpolation algorithm, the 2D data were reconstructed in three dimensions. Our results demonstrate that slice thicknesses up to 4 mm can be used to reliably reconstruct tumours of clinically significant size; the surfaces lay within a 1.5 mm 90%-error margin from each other and the volume difference between the original and reconstructed tumour structures does not exceed 10%. With these settings, Dice coefficients above 0.85 are obtained. The presented interpolation algorithm is able to reconstruct clinically significant tumour structures from 2D histology slices. Errors occurring are in the order of magnitude of common registration artefacts. The method's applicability to real histopathological data is also shown in two resected prostates. An inter-slice spacing of 4 mm or less is recommended during histopathology; the use of a 1.5 mm error margin along the tumour contours can then ensure reliable mapping of the ground truth.

1. Introduction

Imaging of prostate cancer (PCa) is still a challenge. The latest figures show that PCa is the malignancy with the highest incidence and second-highest number of deaths among Western men [1, 2]. Needle biopsy is currently the only method to confirm PCa, but this technique is associated with complications [3] and underdiagnosis due to (aggressive) foci being missed [4]. However, a large fraction of prostatic malignancies are expected to remain clinically insignificant during the patient's lifetime [5]. Hence, there is a substantial clinical demand to develop imaging strategies that are sufficiently accurate to target or even avoid biopsy, and to apply tissue-preserving focal therapy.

In recent years, several magnetic resonance (MR) and ultrasound (US) modalities have been investigated for targeted biopsy, among which multiparametric MR imaging and contrast-enhanced US [6]. In focal therapy, imaging is not only important for localizing the malignancy, but also in risk stratification and to identify insignificant lesions that do not require treatment [7]. The most recent guidelines on focal therapy and trial design indicate that imaging is of vital importance for treatment planning [8, 9]. Moreover, minimally-invasive monitoring methods are required for follow-up after treatment. However, to validate these techniques it is crucial to accurately correlate the images with ground truth information from histopathology.

Histopathology involves the examination of prostate tissue after biopsy or the removal of the gland (i.e., radical prostatectomy (RP)). During the histopathologic procedure after RP, the specimen is usually fixated by immersion in formalin, deprived of the seminal vesicles, and sliced [10]. After the microscopic examination and marking of malignant areas by the pathologist, the slices are digitized. These slices serve as gold standard for distinction between malignant and

© 2017 IOP Publishing Ltd

benign tissue, and allow the pathologist to determine the definitive tumour grade, size, and type [10]. Usually also the tumour volume is assessed, but due to the lack of a simple measurement method it is generally expressed as a percentage of the entire prostate volume [11, 12].

Since images and histology slices are in general not aligned, correlating the two is a complicated task. Moreover, whereas MR images are spaced in a parallel fashion, transrectal US imaging planes may differ in orientation, especially towards basis and apex [13, 14]. The registration process (i.e., the mapping of each location in the RP specimen to the image) is therefore a three-dimensional (3D) problem.

Registration is also important because of the prostate deformations that occur after resection. Comparing *in vivo* with *ex vivo* MR acquisitions, Orzcyk *et al* found that prostates shrink on average by 19.5% [15]. This is most likely caused by the loss of vascular pressure and the absence of in-body connective tissue. The shrinkage is not homogeneously distributed; in particular, the ratio between the anterior–posterior and left–right dimensions decreases after RP. Deformations may also occur as a consequence of the handling of the specimen during fixation and slicing [16]. Furthermore, the shape of the *in vivo* prostate during imaging might be altered by the pressure applied to the prostate because of the use of an endorectal coil in MR imaging [17] or a transrectal probe in US [14].

Many 3D registration methods have been developed for a reliable matching between image data and histopathology. This usually involves the use of landmarks that are manually chosen [18], automatically identified [19], or added after resection [20, 21]. Sometimes *ex vivo* MR [20–24] or elastographic MR images [25] are obtained to facilitate the registration to *in vivo* MR. Alternatively, registration approaches make use of 3D-printed moulds based on 3D imaging [26, 27] or the surface contours of both histology and imaging [14]. Reported registration errors are generally in the order of millimetres.

The accuracy of the validation, however, does not only depend on the ability of the registration algorithm to accurately restore the *in vivo* prostate shape. In the first place, it relies on the ability to reliably reconstruct and digitize the histopathologically examined RP specimen. Almost all registration techniques require a 3D model of the histology slices [14, 18, 22, 23, 27]. For the model reconstruction, the tumour contours have to be interpolated to form 3D structures. In other words, based on the two-dimensional (2D) slices, the entire tumour shape has to be estimated. In all of these steps—slicing, alignment, and tumour interpolation—errors are introduced that complicate the validity of this ground truth.

Figures 1(a)–(c) depict the type of errors occurring during the slicing procedure. Firstly, the sectioning process introduces variations with respect to the inter-slice distance and front-face orientation (i.e., the angle of the slicing plane with respect to the longitudinal axis of the specimen). Gibson *et al* observed these to be distributed with standard deviations of 0.5 mm and 1.1° for a 4.4 mm tissue cutting procedure [28]. In a later study, standard deviations of 0.4 mm and 0.9° were found [29]. Ward *et al* reported a standard deviation of only 0.2 mm for the same slice thickness [20]. Many devices have been developed to standardize the slicing procedure and minimize the errors [16]. However, 88% of the European pathologists cut the RP specimens free-hand [30].

After slicing, the slices have to be re-aligned three-dimensionally (see figure 1(d)). This is usually performed based on block-face photographs (i.e. photos of the RP specimen's front face during slicing) (e.g. [22, 29]). Alignment can also be done using intensity matching of the slices, for example by using mutual information (e.g. [31]). Due to the loss of similarity between slices, however, this method is generally not usable for inter-slice spacings of more than 1 mm [13]. Also the use of natural features such as prostate contours, urethra, or ejaculatory ducts suffers from limited information redundancy and, moreover, most structures are not present in all slices [13]. Lastly, some groups use fiducial markers (sometimes in combination with *ex vivo* MR imaging) to find the original alignment [13, 32, 33]. Although very small errors are reported, this approach is laborious and might deteriorate the specimen. The most common method, still, is manual alignment of the histological slices [34], which introduces significantly more errors than a controlled workflow [35].

For the 3D reconstruction of prostatic malignancy from the 2D slices, the interpolation algorithms reported in the literature range from sparsely stacking the histological data imposed on the photos [22], or simply extrapolating the tumour contour over the entire slice thickness [36, 37], to spline interpolations of the edges [32]. Many other 2D contour-based surface-reconstruction algorithms are designed for medical purposes and might be applied to PCa (e.g. [38–42]). The best choice for interpolation depends on the application, the reliability of the input, and the accuracy required. The need for a smooth interpolation instead of a step-wise approach is often mentioned [32, 43], as well as the list of assumptions underlying 3D modelling (e.g., about slice deformation, parallelity, and location) [29]. Moreover, actual 3D tumour models are very difficult to validate due to the lack of a 3D ground truth.

In this paper, we investigate the effect of the inaccuracies and settings of the slicing procedure on the reliability of the 3D reconstruction. First, we present a method to reconstruct the geometrical tumour structures in 3D based on 2D histopathological data. Then, the reconstruction errors as a result of the slicing procedure are quantified. To this end, we simulate the slicing procedure and compare the result of interpolation with RP phantoms representing a wide range of clinically relevant tumour shapes.

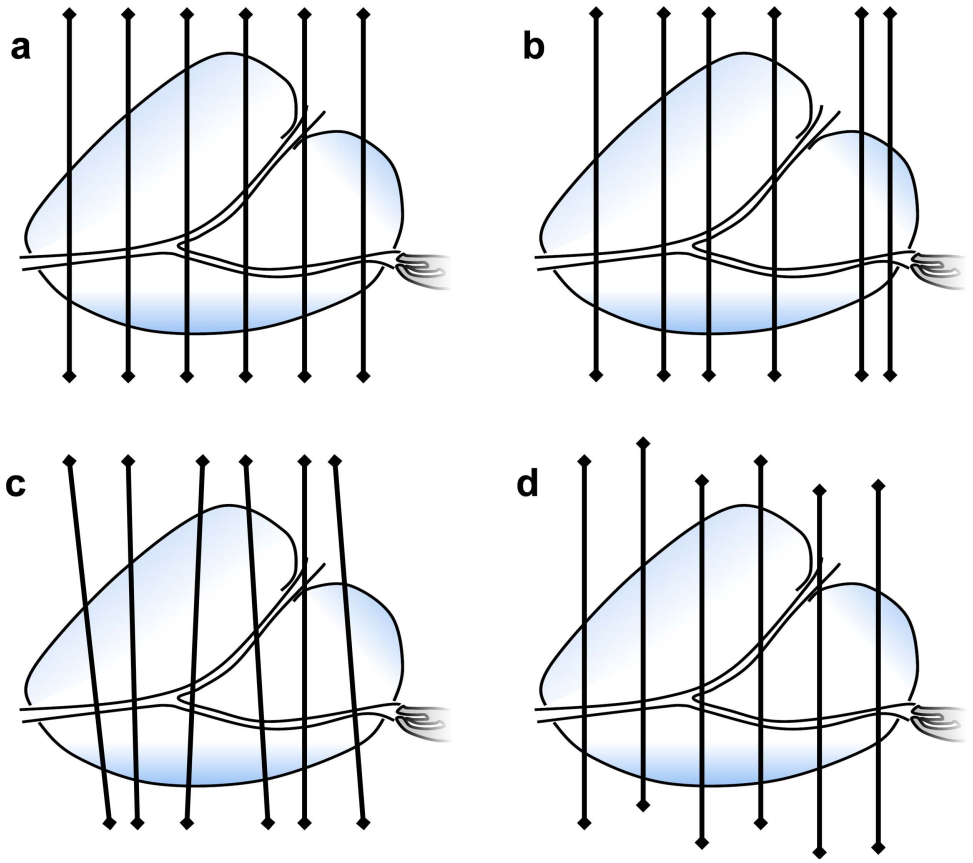

Figure 1. Introduction of errors during the slicing procedure of the radical prostatectomy specimen (in apex-base versus anterior–posterior view): (a) ideal case with equally-spaced, perfectly-aligned, parallel slices; (b) parallel slices of varying slice thickness; (c) equally-spaced slices of varying orientation; (d) equally-spaced and parallel slices that are misaligned.

2. Methods and materials

2.1. Histological procedure

A regular prostatic pathologic examination as described in Montironi *et al* is assumed [10]. In brief, the procedure involves the (a) weighting and sizing of the specimen; (b) inking of the surface to distinguish left and right; (c) (possibly) fixation by 10% neutral-buffered formalin buffer injections; (d) immersion in 300–400 ml of formalin for 24 h; and (e) sectioning by removing the seminal vesicles, dissecting the apical and basal parts and step-slicing the rest of the prostate in ~4 mm sections perpendicular to the apex-base axis. After the sectioning procedure, (f) the slices are post-fixed for 24 h; (g) front-face sections are stained and (h) histologically examined as 5 μm thick slices, either whole-mount or in quadrants. Subsequently, the pathologist prepares the histological slices and draws contours around the malignant areas on each section. These contour data are digitized and properly aligned with respect to each other.

2.2. Interpolation approach

The tumour interpolation and reconstruction algorithms were implemented in Matlab (MathWorks 2015b, Natick, MA). The program retrieves the digital 2D contours and then consecutively (step 1) places them in 3D space; (step 2) determines which contours are likely to belong to the same lesion along several slices; (step 3) estimates enclosing points above or below the contours that are not connected to a contour in an adjacent slice; (step 4) computes the distance points indicating the surface of each lesion using the surface normal vectors; (step 5) interpolates the points to form a distance map using radial basis functions (RBFs) and (step 6) constructs the lesion surfaces at zero-distances. The RBF-approach was chosen due to its characteristic smooth interpolation, versatility and applicability in PCa [44, 45].

2.3. Step 1. Positioning of histological data

The 2D contours of the tumour as determined during the histopathological examination, which have been aligned in the x,y-plane (transverse plane), are placed a slice thickness, d, apart in the z-direction (longitudinal direction).

2.4. Step 2. Identification of independent lesions

Prostatic malignancies are known to be diverse and multifocal [12, 37, 46]. Therefore, it is important to determine whether contours in the histology set belong to the same lesion, or to two independent lesions. In the literature, different criterions are used to select the contours that are to be connected in the interpolation process: for example, Rojas *et al* used a heuristic <5 mm distance between the contours [33] and Erbersdobler

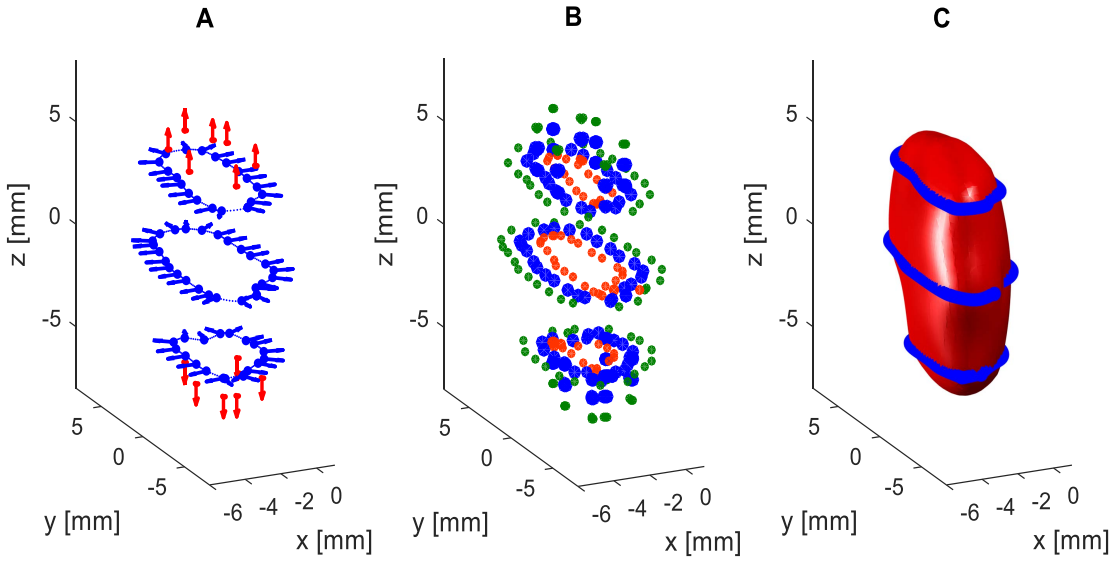

Figure 2. Intermediate steps of interpolation: (A) connected contours (in blue) with top and bottom points (in red) and outward pointing normal vectors; (B) distance map point cloud with on-surface points depicted in blue, inner off-surface points in red and outer off-surface points in green; (C) surface plot of the RBF interpolation.

et al defined <3 mm [47]. In this work, the maximum inter-contour distance is dependent on the used slice thickness. More specifically, it is defined that contour C_k is connected to contour C_l if C_l is in an adjacent slice and if at least one point on the area of C_l is located within a distance $\sqrt{d}$ of the area of C_k in the *x,y*-plane.

This criterion allows us to compute a square matrix M of which each row and column represent a specific contour; a value of 1 is appointed to elements where contour C_k is connected to contour C_l, and a value of 0 where they are not:

$$M(k, l) = \begin{cases} 1 & \text{if } \min(\|C_k(i) - C_l(j)\|) < \sqrt{d} \\ 0 & \text{otherwise} \end{cases}. \quad (1)$$

Here, $||C_k(i) - C_l(j)||$ is the Euclidean distance between point i on the area of contour C_k and point j on the area of contour C_l. Based on the connection matrix M, labels are assigned to all groups of interconnected contours. The number of labels represents the number of separate lesions that will be considered for interpolation individually. In figure 2(A), a typical set of contours forming one lesion is depicted.

2.5. Step 3. Definition of tops and bottoms

Once the labels are assigned, the solid-tumour boundaries are defined by a specific set of 2D contours. The top and bottom of the structures, however, are not considered to be flat. Therefore, additional top and bottom points are positioned under and above the lowest and upper contour, respectively.

For small contours, these top and bottom points are placed at the centre of mass of the adjacent contour C, half the slice thickness d away. This is based on the assumption that, in the absence of more information, lesions probably reach half the distance between the contour and the next, empty slice.

Heuristically, if the average distance between the points on C and its centre of mass differ by more than 1 mm, the contours are divided in n different k-means clusters for which top or bottom points are added in their centre of mass at $d/4$. This number n depends on the standard deviation (σ) in distances to the centre of mass via the expression $n = 1 + \lceil 3\sigma/2 \rceil$. This formula ensures that top or bottom contours that are large or less circular are more rigorously enclosed. These additional points are also visible in figure 2(A).

2.6. Step 4. Definition of seed points using surface normal vectors

Each tumour structure is now enclosed by its contours and top and bottom points. This can be viewed as a 3D point cloud defining the lesion's surface. Following the method described by Carr *et al* [45] and used by [44, 48], it is possible to reconstruct the outer surface of the prostate by RBF interpolation. We refer to [45] for the mathematical foundations of the algorithm.

The interpolation algorithm does not only require the points on the surface (on-surface points) as input, but also points at a certain distance from the surface (off-surface points). More specifically, it has been shown that the problem is more straightforward to solve when two off-surface points are defined on either side of each on-surface point. Points inside of the structure are marked with its negative distance to the surface, whereas points on the outside have a positive distance value. Generating such a set of distance points is a critical task, given the wide range of complex contour shapes. In the presented method, given the contour shapes encountered, it was possible to reduce the number of points on the contour circumference to one

point every ~1 mm in order to reduce the computation time. In our case, this meant a reduction by 5/6.

Considering the typical dimensions of PCa lesions, off-surface points are added at approximately 1 mm on either side of the surface as shown in figure 2(B). Their positions are computed using the normal vectors in the contour plane. It is not uncommon to encounter contours of which the centre of mass is located outside the tumour area; therefore, their outward direction is verified by calculating the number of intersections between the normal line and the contour: an odd number of intersections in the direction of the normal vector cannot occur. For all top and bottom points that are added in the previous step, the normal vectors will point in the outward longitudinal direction (see figure 2(A)). Since these 1 mm distances must not intersect other parts of the contour, the algorithm might fail in reconstructing contours that have very sharp edges or lie in a close range to each other. In these rare cases, the distance settings should be adjusted.

2.7. Step 5. Interpolation by RBFs

Based on the set of distance points, the interpolation algorithm is used to compute a so-called 3D distance map. In this map, the distance to the lesion's surface at any location can be found. In order to create a smooth distance map, each distance point is allowed to deviate from its original value. The extent of this deviation is controlled by a smoothing parameter, ρ, which is heuristically set to 0.001 [45]. This low value was adopted, as we do not allow our histologic data to deviate much from the pathologist's 2D delineations in order to make smoother structures [49].

2.8. Step 6. Isosurfacing of the distance map

Since the distance map contains the interpolated distance to the lesion's surface at every location, the shape of the lesion is now defined by all locations at which the map is equal to zero. An example of the interpolation result is shown in figure 2(C).

2.9. *In silico* phantoms

In order to quantify the interpolation errors, the entire slicing and reconstruction process was simulated using digital phantoms. This does not only solve the absence of a 3D ground truth volume *in vivo* and *in vitro*, but it also enabled us to separately study the effects of variations in slice thickness, front-face orientation, and alignment. Furthermore, it allows many different experiments on a single phantom. Obviously, it is of paramount importance that the phantom designs represent the spectrum of frequently encountered PCa shapes as well as possible.

Over the years, several distribution maps have been created that show that PCa is most often found in the peripheral zone (74%) and, therefore, in the lower, posterior regions of the prostate [33, 37, 46, 50]. Lesions often have predictable smooth shapes, especially since small lesions are known to spread along the prostatic and zonal boundaries (94%) [37]. Most lesions of more than 1 ml in volume (83%) are found to be roughly diamond-shaped in longitudinal (apex-base) direction [37].

A large majority (83%) of the RP specimens exhibits multiple foci [46]. In these cases, the non-index (i.e., not largest) PCa foci most often (69%) occur on the opposite side of the index-tumour [37]. Furthermore, transition-zone tumours are almost always associated with well differentiated peripheral index tumours [46]. In general, the index lesion determines the prognosis [7].

Typically, PCa lesions of >0.5 ml are considered clinically significant [7, 37]. It was found by Frimmel *et al* that the tumour volume in resected prostates is, on average, 3.67 ml. Based on their volume, the lesions have been subdivided in small (0.3–1.6 ml), medium (1.6–3.6 ml) and large (3.8–36.2 ml) tumours [50]. In this work, the focus is on the small and medium-sized structures, because small foci are most frequently found [46]. Moreover, large tumours are more easily interpolated because they appear in more histological slices and slicing errors are relatively small compared to their size.

With the aim of representing clinically relevant shapes, we designed eight different tumour structures that are generally difficult to interpolate (see figure 3). Phantom A1 (total tumour volume of 2.1 ml) consists of four spheres of 10 mm in diameter, representing the most confined shape of clinically significant size (0.5 ml). Phantoms A2 (1.1 ml) and A3 (0.44 ml) contain the same architecture of spheres with sub-clinically relevant diameters of 8 mm and 6 mm, respectively. Phantom B (3.4 ml) consists of two independent lesions of significant size that are more than 3 mm but less than 5 mm apart; this is the smallest significant gap for which two tumours are considered independent [47]. Phantom C (1.7 ml) consists of two similarly-sized structures of which one is oriented along the slicing direction and the other one is oriented in the transverse plane. Since both structures are slightly tilted, errors occurring due to the 'shear effect' are elegantly shown. This effect indicates the inability to identify ill-alignment in interpolating 2D-slices [13]. Phantom D (3.3 ml) harbours two semi-toroid structures that appear as two separate contours in some slices, whereas they are joined in others. Phantom E (2.6 ml) contains similar structures, but now another unconnected structure is added. Lastly, phantom F (3.0 ml) shows a single tumour structure with a hole. These last three phantoms verify the validity of the decision rule in connecting contours [33].

Prostate outlines were added to the phantoms in order to show how the tumour dimensions relate to the size of a typical prostate. It concerns an ellipsoid shape of 48, 34.2 and 40 mm along the main axes. After triangulation, the structure has a volume of 31.9 ml, which is equal to the average volume of RP specimens [50].

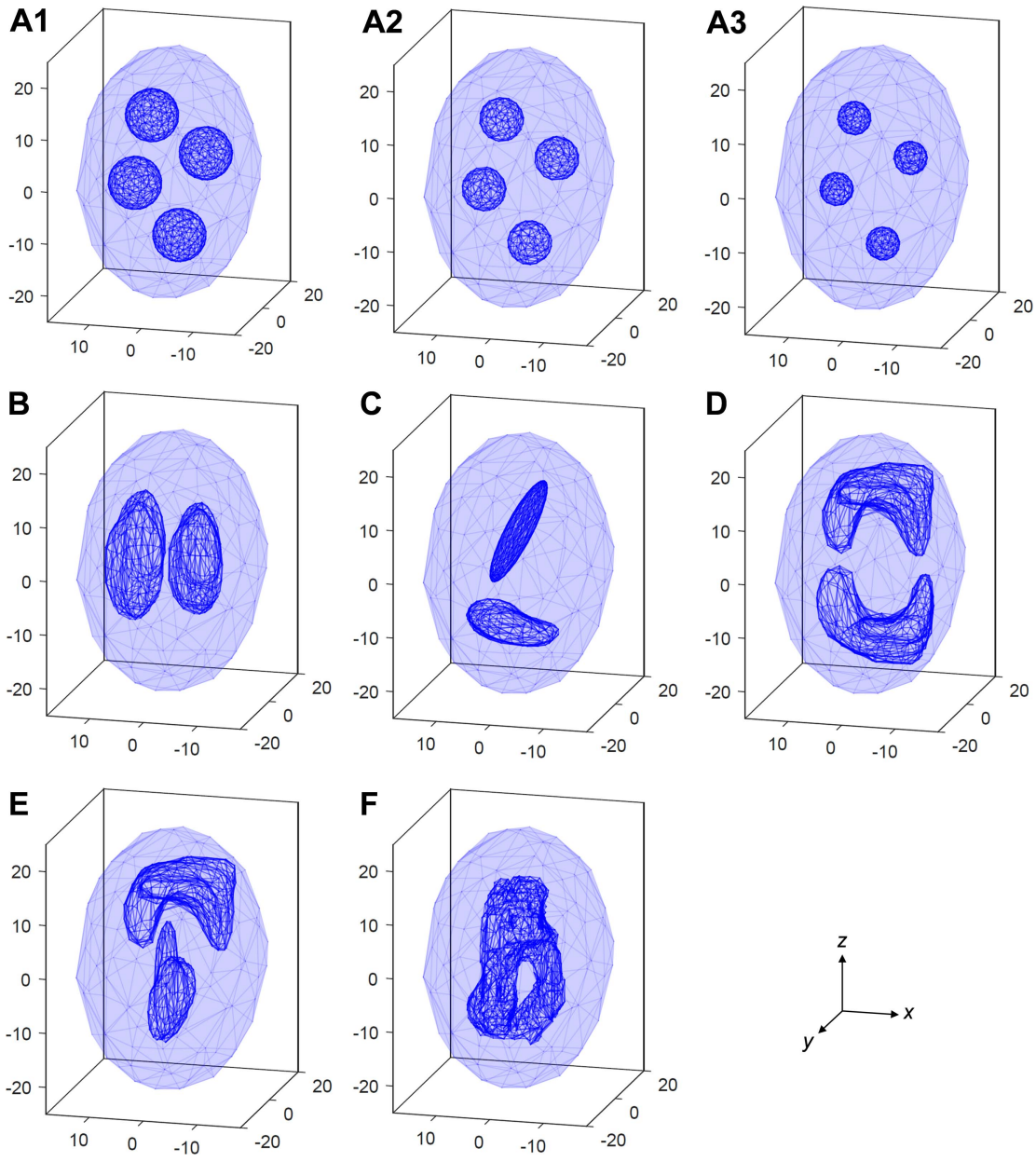

Figure 3. Depiction of the 3D prostate-tumour phantoms used in this work. All phantoms have a 24 × 17.1 × 20 mm radii ellipsoid prostate boundary. (A1)–(A3) consist of four spherical lesions with a radius of 5, 4, and 3 mm, respectively; (B) represents two clinically relevant tumour foci with a gap of less than 5 mm in between; (C) contains two tumour foci with different orientation with respect to the longitudinal plane; (D) consists of two semi-toroid structures; (E) harbours a semi-toroid with another structure in between; (F) contains a single structure with a hole.

2.10. Validation and quantification

The phantoms depicted in figure 3 underwent a virtual slicing procedure by computing the cross-sections of the phantom with planes that were positioned a slice thickness d apart in the longitudinal (z) direction. For each simulation, these locations were all randomly displaced according to a normal distribution with a standard deviation of 0.5 mm, that is, the largest reported in the literature [28]. In order to quantify the effect of misorientation, the planes were placed under an angle $0 \pm \alpha_{\text{std}}^{\circ}$ around to the y-axis. The errors resulting from misalignments were assessed by random displacements $0 \pm w_{\text{std}}$ mm in the x- and y-directions. Subsequently, the phantom contours were extracted, interpolated, and reconstructed assuming a perfect slicing procedure with the given slice thickness (i.e., no displacements, misorientation, and misalignments). An example of a slicing and reconstruction procedure is shown in figure 4.

Each simulation sequence was executed 15 times to show the effect of the randomness and to rule out incidental findings. Simulations in which the interpolation algorithm failed to find a closed solution were excluded (<4%). To assess the quality of the reconstruction, the fractional volume difference (FVD) was calculated: the volume difference between reconstruction ($\boldsymbol{V}_{\text{rec}}$) and original phantom ($\boldsymbol{V}_{\text{ref}}$) as a fraction of

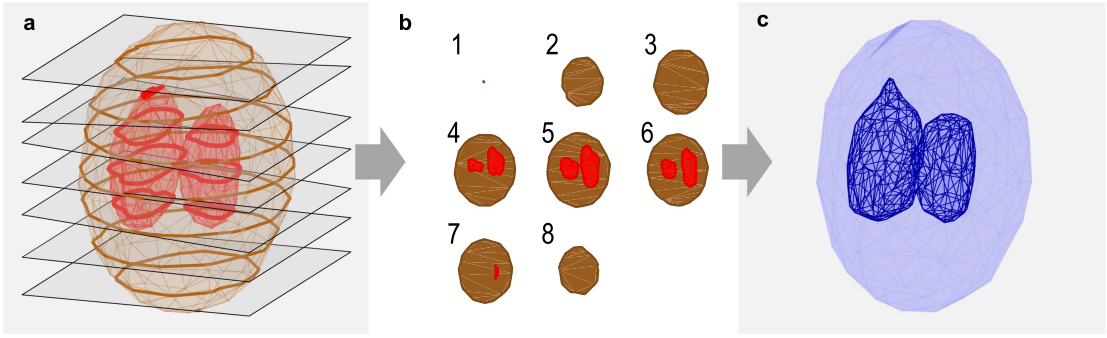

Figure 4. Virtual slicing procedure; (a) slicing of the digital phantom (6 mm); (b) simulated histological slices; (c) resulting reconstruction of the original phantom based on the slices.

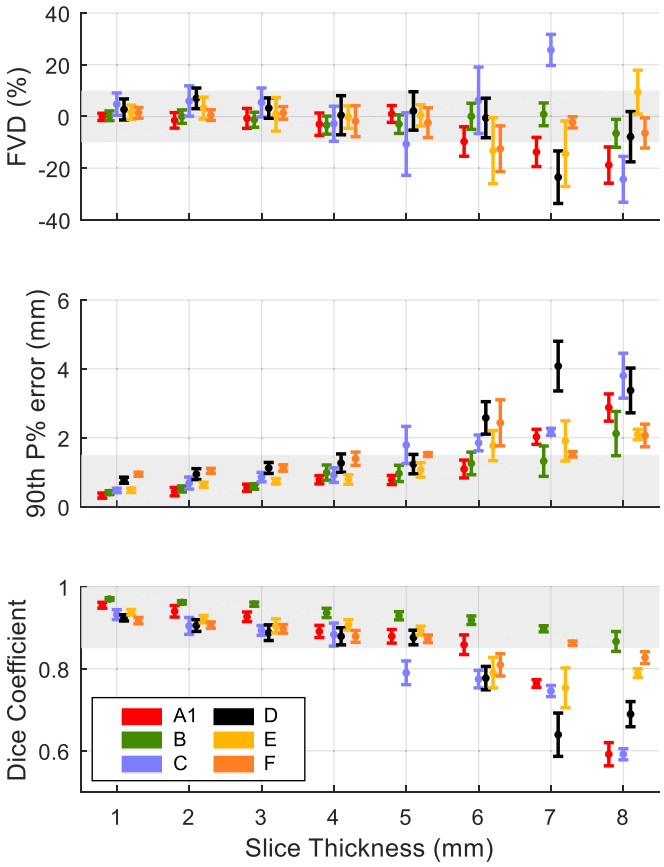

Figure 5. Mean fractional volume difference (FVD), 90th percentile value of the error distance (90th P%), and Dice coefficient of 15 sectioning simulations of phantom (A1)–(F) versus the slice distance $d \pm 0.5$ mm. The error bars indicate the standard deviation among the results.

the original phantom volume:

$$\mathrm{FVD} = (|V_{\mathrm{rec}}| - |V_{\mathrm{ref}}|)/|V_{\mathrm{ref}}| \quad (2)$$

in which $|V|$ represents the volume of V.

In addition, the reconstruction errors were quantified by the shortest distance between the outer surface of the original phantom and that of the reconstruction. More specifically, the 90th percentile of the reconstruction errors are mentioned. This means that 90% of the points on the original surface and the corresponding reconstruction surface are within an error margin of the given value.

Lastly, the overlap between reference and reconstruction was studied using the Dice coefficient, which defines the relative volume shared by reconstruction and reference as follows [23]:

$$D = 2(|V_{\mathrm{rec}} \cap V_{\mathrm{ref}}|)/(|V_{\mathrm{ref}}| + |V_{\mathrm{rec}}|). \quad (3)$$

3. Results

3.1. Slice thickness

Figure 5 depicts the interpolation performance versus the slice thickness $d \pm 0.5$ mm. It is observed that, for

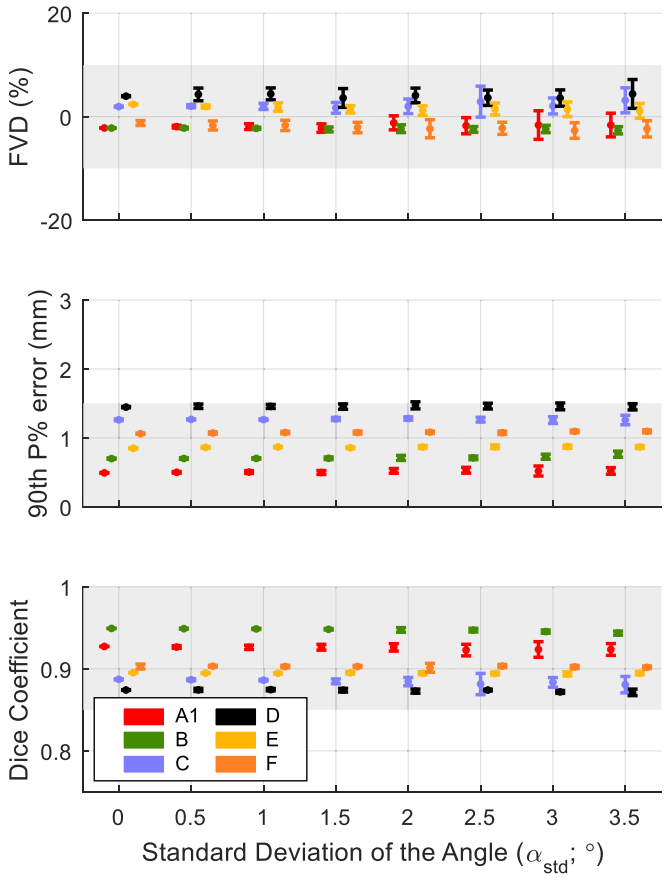

Figure 6. Mean fractional volume difference (FVD), 90th percentile value of the error distance (90th P%), and Dice coefficient of 15 sectioning simulations of phantom (A1)–(F) with 4 mm slices oriented under an angle of $0 \pm \alpha_{std}$° as function of the standard deviation. The error bars indicate the standard deviation among the results.

slice thicknesses up to 4 mm, the means and standard deviations of the performance measures stay virtually constant. They exhibit error margins below 1.5 mm, FVD within 10% from baseline, and Dice coefficient above 0.85 (see grey regions). Some tumour designs appear to be generally more difficult to interpolate. From slice thicknesses >4 mm, the performance measures and standard deviations degrade rapidly and are less predictable. This is because the position of the slices with respect to the tumour structure is increasingly important; for example, a small deviation in an 8 mm slicing sequence might lead to missing entire tumour foci.

3.2. Slice orientation

To quantify the effect of non-parallel slicing, the angle of the transversal cross-sections in a 4 mm equidistant slicing sequence was randomly adjusted by $0 \pm \alpha_{std}$° around the *y*-axis. In figure 6, it is shown that an increasing α_{std} does not result in a large difference in means with respect to the parallel sequence, but it affects the standard deviations of the results. This is due to an equal probability of cross-sections appearing somewhat larger or somewhat smaller than they should.

3.3. Slice alignment

The interpolation requires the 2D contours to be spatially aligned in 3D in order to reconstruct the original shape. Due to the sparsity of the data in the longitudinal direction, misalignment is a recurring problem in 3D reconstruction which is difficult to identify or avoid without additional information. As can be seen in figure 7, displacements of $0 \pm w_{std}$ mm in the *x*, *y*-plane affect the Dice coefficient to a larger extent than the other performance measures. This is because reconstructed structures may maintain their original shape and volume, while shifting from the original position. Random misalignment of more than 1.5 mm introduces large performance drops.

3.4. Tumour size

Considering only the spherical phantoms (A1)–(A3), roughly the same effects as for the other designs are seen. It becomes clear from figure 8 that the errors are generally largest for the smallest lesions, as well as the variety (standard deviations) in their results. Therefore, sub-clinically relevant structures smaller than 0.25 ml are not expected to be well interpolated for large inter-slice spacings of ⩾4 mm.

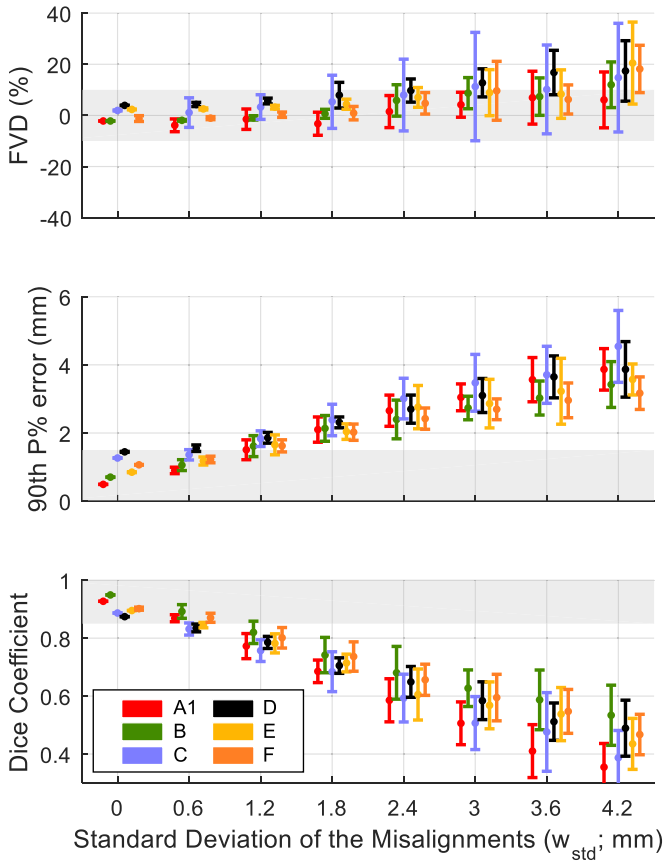

Figure 7. Mean fractional volume difference (FVD), 90th percentile value of the error distance (90th P%), and Dice coefficient of 15 sectioning simulations of phantom (A1)–(F) with parallel 4 mm slices that are misaligned in the transverse plane by $\Delta x = \Delta y = 0 \pm w_{\text{std}}$ mm as function of the misalignment standard deviation. The error bars indicate the standard deviation among the results.

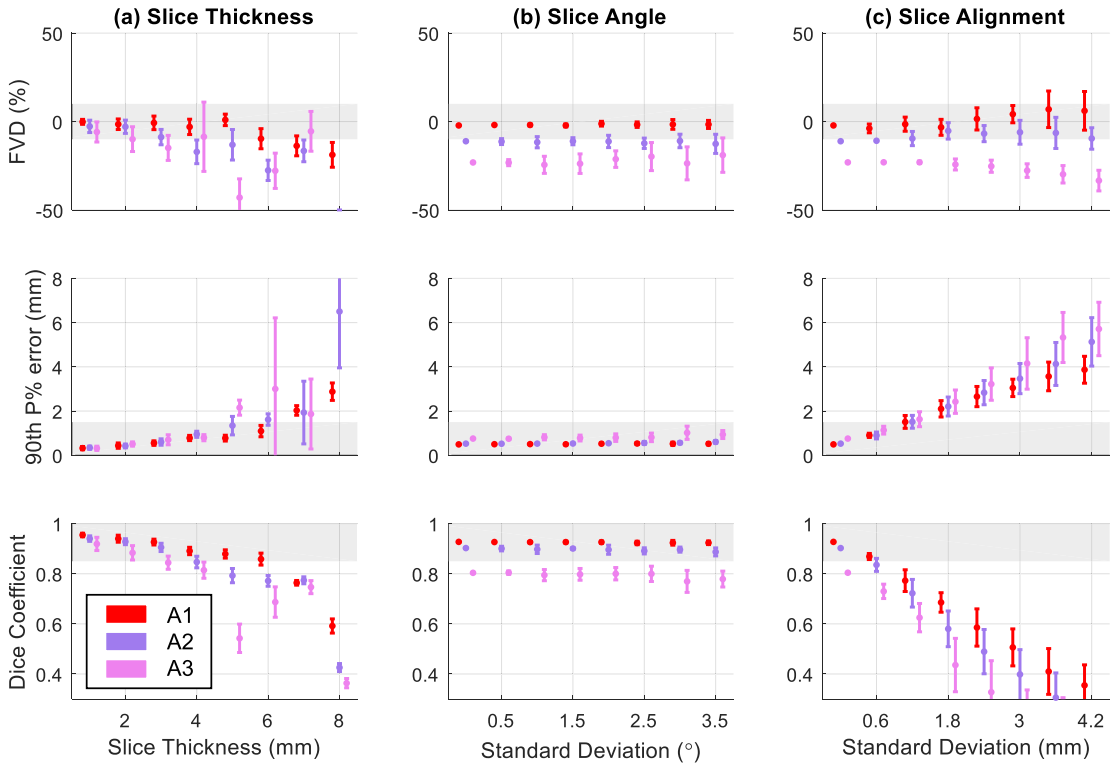

Figure 8. Mean fractional volume difference (FVD), 90th percentile value of the error distance (90th P%), and Dice coefficient of 15 sectioning simulations of phantom (A1)–(A3) with (a) parallel slicing distances of $d \pm 0.5$ mm, (b) 4 mm slicing under an angle $0 \pm \alpha_{\text{std}}°$ and (c) misalignments in the transverse plane by $\Delta x = \Delta y = 0 \pm w_{\text{std}}$ mm.

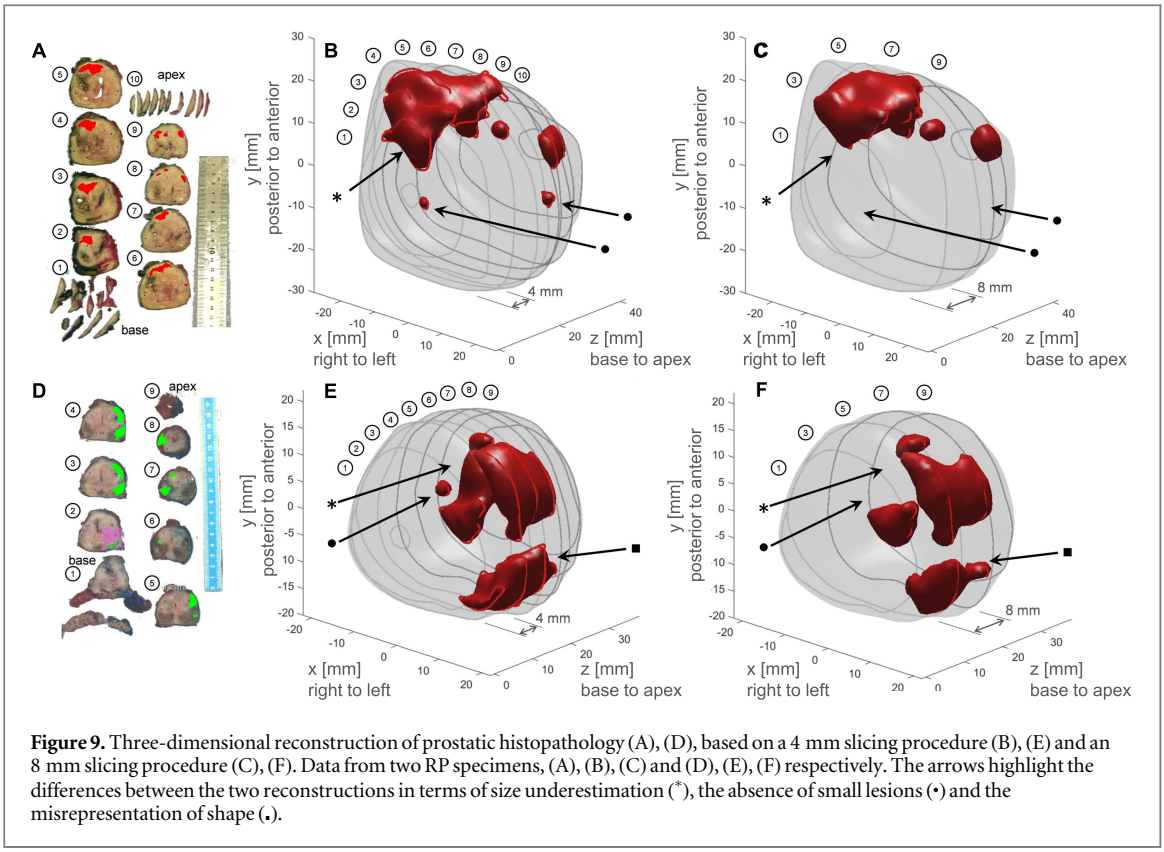

Figure 9. Three-dimensional reconstruction of prostatic histopathology (A), (D), based on a 4 mm slicing procedure (B), (E) and an 8 mm slicing procedure (C), (F). Data from two RP specimens, (A), (B), (C) and (D), (E), (F) respectively. The arrows highlight the differences between the two reconstructions in terms of size underestimation (*), the absence of small lesions (•) and the misrepresentation of shape (▪).

3.5. 3D reconstruction of patient pathology

To illustrate the applicability of the described interpolation method, we applied the presented method to actual pathology data. The RP specimens were collected in the Academic Medical Center (Amsterdam, The Netherlands) for an approved study with informed consent. The prostate and tumour contours were delineated by a pathologist and subsequently digitized, aligned, and used to reconstruct the histopathology. In accordance with the above protocol, a slice thickness of 4 mm was adopted. In figure 9, the histopathology slices and their 3D reconstruction are shown. We also conducted the 3D reconstruction based on an 8 mm slicing procedure, by only taking into account every other slice. These results, shown alongside the 4 mm models, clearly demonstrate the effects predicted in section 3.1; for slice distances >4 mm, tumour structures are underestimated in size (see the arrows indicated with *), small lesions are missed (see arrows indicated with •), and tumour shapes are not well-captured (see arrows indicated with ▪).

4. Discussion

Because of the demand for imaging validation and the development of 3D imaging modalities, an accurate 3D model from the RP specimen becomes increasingly important. Nowadays, validation with histopathology is performed by matching 2D imaging planes with corresponding 2D histological slices, or by registration of the 3D volumes [34]. Because histological slices and imaging planes cannot be considered to be completely overlapping and aligned, the second approach is favourable, provided that the 3D reconstruction is sufficiently accurate. Considering the dimensions of the prostate, small errors in the slicing procedure have relatively large effects. In this work, these effects were quantified, allowing us to determine the required accuracy in the pathology workflow for reliable 3D reconstruction.

We described and tested a RBF-based algorithm to reconstruct the tumour structures from a series of 2D histopathologic slices. Using *in silico* phantoms representing frequently encountered tumour structures, we demonstrated that slice thicknesses up to 4 mm can be used to reconstruct tumours of clinically significant size with an appreciable accuracy; the surfaces deviate within a 1.5 mm 90%-error margin, the volume difference between reference and reconstruction does not exceed 10%, and a Dice coefficient above 0.85 is maintained.

This study was performed *in silico*, as it enabled us to repeat the slicing procedure with different values and ensured a valid ground truth. This way, it was possible to rule out incidental findings caused by fortunate or unfortunate positioning of the slices with respect to the lesions. Preferably, the tumour appears in as many cross-sections as possible, so that the overall tumour shape is best represented. Since the tumour shape is not known beforehand, the suitability of the set of contours depends on the initial slicing location. It should therefore be noted that there is an intrinsic

variation in the outcomes of every slicing procedure. This effect was demonstrated using histopathology datasets of two RP specimens.

A limitation of the procedure is that the occurrence of errors was simulated as a random process. Depending on the details of the histopathology procedure, systematic errors can be expected in slicing and alignment. For example, one might find the standard deviation of the angle to be dependent on slice thickness or location in the prostate. However, when making use of cutting devices, this error remains constant. Also the slicing direction (i.e., apex-base or vice versa) might have an influence; due to the cumulative errors in slice thickness, the location of the first slice could be more accurate than the last one. Furthermore, it was observed that slicing itself might introduce tears, deformations and inconsistencies that are not modelled here [16].

Since the algorithm uses criteria regarding inter-contour connection and top and bottom heights, the procedure can be optimized to best suit the evaluation at hand. The false positive or false negative volumes can be reduced by using a more conservative or loose decision rule, respectively. Ultimately, more elaborate and robust decision rules can be devised that take into account the lesion volumes and contour shapes.

Since 4 mm slicing distances were found to be sufficient, the algorithm does not require the pathologist to perform a more elaborate and laborious protocol for the histological examination. Furthermore, although the computation time for interpolation depends on the number of contours and data points, the reconstruction generally takes around 1–2 min (using one core on a 3.40 GHz quad-core processor personal computer).

Whereas slight deviations in front-face angle did not substantially alter the reconstruction for clinically significant PCa lesions, the inter-slice misalignment significantly affected the interpolation performance. This underlines the need for an alignment strategy such as the use of fiducial markers or block-face photographs. Recent alignment strategies have shown to reduce misalignment distances to 0.6 mm [13].

It was demonstrated that the errors made in tumour interpolation are in the same order of magnitude as the registration errors (e.g., 1.1 mm [20], 0.71 mm [21], 2–3 mm [18], 0.82 mm [19], 2.26–3.74 mm [22], 3.1 mm [25], 1.5–2.1 mm [14]). Nevertheless, the total error in matching histopathologically-confirmed tumour structures with images is not simply an addition of these errors. Especially in elastic registration, the registration process might even compensate for misalignments in interpolation. Since tumours tend to spread along the prostatic capsule [37], especially surface-based registration algorithms could correct tumour misalignments. In any case, the quantified errors of this study indicate that caution should be taken in interpreting the histopathological data within 1.5 mm from delineated borders of areas marked as malignant.

Despite some debate, the total tumour volume is generally regarded as a valuable prognostic marker [11, 12], particularly for biochemical recurrence after RP [51]. Current protocols include extensive stereological methods to estimate the volume, but these methods have some well-known limitations in labour and time involved [12]. The presented interpolation method is found to estimate the volumes with less than 10% offset for the average standard histopathology protocol.

Furthermore, the technique is not limited to the prostate alone and might be used for other small organs, in particular those that do not have usable internal natural markers. Similar reconstruction protocols have been developed for the (animal) brain [40]. However, the optimal slicing thickness, location of seed points and decision rules should be tailored to the dimensions and requirements of that organ.

In conclusion, we presented a 3D interpolation algorithm that is able to reconstruct PCa tumour structures based on 2D histopathologic slices and quantified to what extent this is affected by errors in the pathology procedure in terms of slicing distance, slicing angle and misalignments. It was demonstrated that an inter-slice distance up to 4 mm permits reliable use of 3D histology as gold standard. A good reconstruction of the 3D tumour shape enables the validation of cancerous representation in novel imaging modalities with high precision. With accurate tumour localization, the validation is no longer limited to large tumours or quadrants. More patients may be enrolled in studies when tumours of all shapes and sizes can be reliably used for validation, increasing the statistical outcomes of the validation.

Acknowledgments

This study has been performed in the framework of the IMPULS2-program within the Eindhoven University of Technology in collaboration with Philips. It was also supported by the European Research Council Starting Grant (#280209) as well as a grant from the Dutch Cancer Society (#UVA2013-5941).

References

[1] American Cancer Society 2015 *Cancer Facts and Figures 2015* (Atlanta, GA: American Cancer Society)
[2] American Cancer Society 2012 *Global Cancer Facts and Figures* 3rd edn (Atlanta, GA: American Cancer Society) pp 1–64
[3] Loeb S, Vellekoop A, Ahmed H U, Catto J, Emberton M, Nam R, Rosario D J, Scattoni V and Lotan Y 2013 Systematic review of complications of prostate biopsy *Eur. Urol.* **64** 876–92
[4] Ukimura O *et al* 2013 Contemporary role of systematic prostate biopsies: indications, techniques, and implications for patient care *Eur. Urol.* **63** 214–30
[5] Bangma C H, Roemeling S and Schröder F H 2007 Overdiagnosis and overtreatment of early detected prostate cancer *World J. Urol.* **25** 3–9
[6] van Hove A, Savoie P-H, Maurin C, Brunelle S, Gravis G, Salem N and Walz J 2014 Comparison of image-guided targeted biopsies versus systematic randomized biopsies in the detection of prostate cancer: a systematic literature review of well-designed studies *World J. Urol.* **32** 847–58

[7] Orczyk C, Emberton M and Ahmed H U 2015 What tumours should we treat with focal therapy based on risk category, grade, size and location? *Curr. Opin. Urol.* **25** 212–9
[8] van den Bos W *et al* 2014 Focal therapy in prostate cancer: international multidisciplinary consensus on trial design *Eur. Urol.* **65** 1078–83
[9] De la Rosette J, Ahmed H, Barentsz J, Johansen T B, Brausi M, Emberton M, Frauscher F, Greene D, Harisinghani M and Haustermans K 2010 Focal therapy in prostate cancer—report from a consensus panel *J. Endourol.* **24** 775–80
[10] Montironi R, van der Kwast T, Boccon-Gibod L, Bono A V and Boccon-Gibod L 2003 Handling and pathology reporting of radical prostatectomy specimens *Eur. Urol.* **44** 626–36
[11] Buhmeida A, Pyrhönen S, Laato M and Collan Y 2006 Prognostic factors in prostate cancer *Diagn. Pathol.* **1** 1–15
[12] Montironi R, Mazzucchelli R and van der Kwast T 2003 Morphological assessment of radical prostatectomy specimens. a protocol with clinical relevance *Virchows Arch.* **442** 211–7
[13] Hughes C, Rouviere O, Mege-Lechevallier F, Souchon R and Prost R 2013 Robust alignment of prostate histology slices with quantified accuracy *IEEE Trans. Biomed. Eng.* **60** 281–91
[14] Schalk S G, Postema A, Saidov T A, Demi L, Smeenge M, de la Rosette J J M C H, Wijkstra H and Mischi M 2016 3D surface-based registration of ultrasound and histology in prostate cancer imaging *Comput. Med. Imaging Graph.* **47** 29–39
[15] Orczyk C, Taneja S S, Rusinek H and Rosenkrantz A B 2014 Assessment of change in prostate volume and shape following surgical resection through co-registration of *in vivo* MRI and fresh specimen *ex vivo* MRI *Clin. Radiol.* **69** e398–403
[16] Chen L H, Ho H, Lazaro R, Thng C H, Yuen J, Ng W S and Cheng C 2010 Optimum slicing of radical prostatectomy specimens for correlation between histopathology and medical images *Int. J. Comput. Assist. Radiol. Surg.* **5** 471–87
[17] Heijmink S W, Scheenen T W J, van Lin E N J T, Visser A G, Kiemeney L A L M, Witjes J A and Barentsz J O 2009 Changes in prostate shape and volume and their implications for radiotherapy after introduction of endorectal balloon as determined by MRI at 3T *Int. J. Radiat. Oncol. Biol. Phys.* **73** 1446–53
[18] Groenendaal G, Moman M R, Korporaal J G, van Diest P J, van Vulpen M, Philippens M E P and van der Heide U A 2010 Validation of functional imaging with pathology for tumor delineation in the prostate *Radiother. Oncol.* **94** 145–50
[19] Zhan Y, Ou Y, Feldman M, Tomaszeweski J, Davatzikos C and Shen D 2007 Registering histologic and Mr images of prostate for image-based cancer detection *Acad. Radiol.* **14** 1367–81
[20] Ward A D, Crukley C, McKenzie C A, Montreuil J, Gibson E, Romagnoli C, Gomez J A, Moussa M, Chin J and Bauman G 2012 Prostate: registration of digital histopathologic images to *in vivo* MR images acquired by using endorectal receive coil *Radiology* **263** 856–64
[21] Gibson E, Crukley C, Gaed M, Gómez J A, Moussa M, Chin J L, Bauman G S, Fenster A and Ward A D 2012 Registration of prostate histology images to *ex vivo* MR images via strand-shaped fiducials *J. Magn. Reson. Imaging* **36** 1402–12
[22] Park H, Piert M R, Khan A, Shah R, Hussain H, Siddiqui J, Chenevert T L and Meyer C R 2008 Registration methodology for histological sections and *in vivo* imaging of human prostate *Acad. Radiol.* **15** 1027–39
[23] Orczyk C, Rusinek H, Rosenkrantz A B, Mikheev A, Deng F-M, Melamed J and Taneja S S 2013 Preliminary experience with a novel method of three-dimensional co-registration of prostate cancer digital histology and *in vivo* multiparametric MRI *Clin. Radiol.* **68** e652–8
[24] Reynolds H M *et al* 2015 Development of a registration framework to validate MRI with histology for prostate focal therapy *Med. Phys.* **42** 7078–89
[25] Nir G, Sahebjavaher R S, Kozlowski P, Chang S D, Sinkus R, Goldenberg S L and Salcudean S E 2013 Model-based registration of *ex vivo* and *in vivo* MRI of the prostate using elastography *IEEE Trans. Med. Imaging* **32** 1068–80
[26] Shah V, Pohida T, Turkbey B, Mani H, Merino M, Pinto P A, Choyke P and Bernardo M 2009 A method for correlating *in vivo* prostate magnetic resonance imaging and histopathology using individualized magnetic resonance-based molds *Rev. Sci. Instrum.* **80** 104301
[27] Priester A, Natarajan S, Le J D, Garritano J, Radosavcev B, Grundfest W, Margolis D J A, Marks L S and Huang J 2014 A system for evaluating magnetic resonance imaging of prostate cancer using patient-specific 3D printed molds *Am. J. Clin. Exp. Urol.* **2** 127–35
[28] Gibson E, Gómez J A, Moussa M, Crukley C, Bauman G, Fenster A and Ward A D 2012 3D reconstruction of prostate histology based on quantified tissue cutting and deformation parameters *Proc. SPIE* **8317** 83170N
[29] Gibson E, Gaed M, Gómez J A, Moussa M, Pautler S, Chin J L, Crukley C, Bauman G S, Fenster A and Ward A D 2013 3D prostate histology image reconstruction: quantifying the impact of tissue deformation and histology section location *J. Pathol. Inform.* **4** 31
[30] Egevad L 2012 Handling of radical prostatectomy specimens *Histopathology* **60** 118–24
[31] Ou Y, Shen D, Feldman M, Tomaszewski J and Davatzikos C Non-rigid registration between histological and MR images of the prostate: a joint segmentation and registration framework *Computer Vision and Pattern Recognition (CVPR) Workshop: Mathematical Methods in Biomedical Image Analysis (MMBIA) (Miami, FL)* pp 125–32 http://repository.upenn.edu/be_papers/141/
[32] Taylor L S, Porter B C, Nadasdy G, di Sant'Agnese P A, Pasternack D, Wu Z, Baggs R B, Rubens D J and Parker K J 2004 Three-dimensional registration of prostate images from histology and ultrasound *Ultrasound Med. Biol.* **30** 161–8
[33] Rojas K D *et al* 2015 Methodology to study the three-dimensional spatial distribution of prostate cancer and their dependence on clinical parameters *J. Med. Imaging* **2** 37502
[34] Xiao G, Bloch B N, Chappelow J, Genega E M, Rofsky N M, Lenkinski R E, Tomaszewski J, Feldman M D, Rosen M and Madabhushi A 2011 Determining histology-MRI slice correspondences for defining MRI-based disease signatures of prostate cancer *Comput. Med. Imaging Graph.* **35** 568–78
[35] Yamamoto H, Nir D, Vyas L, Chang R T, Popert R, Cahill D, Challacombe B, Dasgupta P and Chandra A 2014 A workflow to improve the alignment of prostate imaging with whole-mount histopathology *Acad. Radiol.* **21** 1009–19
[36] Malone S C, Haridass A, Nyiri B, Croke J, Malone C, Breau R H, Morash C, Avruch L, Daneshmand M and Malone K 2014 Creation of three-dimensional prostate cancer maps: methodology and clinical and research implications *Arch. Pathol. Lab. Med.* **138** 803–8
[37] Haffner J, Potiron E, Bouyé S, Puech P, Leroy X, Lemaitre L and Villers A 2009 Peripheral zone prostate cancers: location and intraprostatic patterns of spread at histopathology *Prostate* **69** 276–82
[38] Albu A B, Beugeling T and Laurendeau D 2008 A morphology-based approach for interslice interpolation of anatomical slices from volumetric images *IEEE Trans. Biomed. Eng.* **55** 2022–38
[39] Kels S and Dyn N 2011 Reconstruction of 3D objects from 2D cross-sections with the 4-point subdivision scheme adapted to sets *Comput. Graph.* **35** 741–6
[40] Ourselin S, Roche A, Subsol G, Pennec X and Ayache N 2001 Reconstructing a 3D structure from serial histological sections *Image Vis. Comput.* **19** 25–31
[41] Li Y, Shin J, Choi Y and Kim J 2015 Three-dimensional volume reconstruction from slice data using phase-field models *Comput. Vis. Image Underst.* **137** 115–24
[42] Werahera P N, Miller G J, Taylor G D, Brubaker T, Daneshgari F and Crawford E D 1995 A 3D reconstruction algorithm for interpolation and extrapolation of planar cross sectional data *IEEE Trans. Med. Imaging* **14** 765–71
[43] Salarian M, Shahedi M, Gibson E, Gaed M, Gómez J A, Moussa M, Bauman G S and Ward A D 2013 Toward quantitative digital histopathology for prostate cancer: comparison of inter-slide interpolation methods for tumour measurement *Proc. SPIE* **8676** 86760F

[44] Cool D, Downey D, Izawa J, Chin J and Fenster A 2006 3D prostate model formation from non-parallel 2D ultrasound biopsy images *Med. Image Anal.* **10** 875–87
[45] Carr J C, Beatson R K, Cherrie J B, Mitchell T J, Fright W R, McCallum B C and Evans T R 2001 Reconstruction and representation of 3D objects with radial basis functions *Proc. 28th Annual Conf. on Computer Graphics and Interactive Techniques* pp 67–76
[46] Chen M E, Johnston D A, Tang K, Babaian R J and Troncoso P 2000 Detailed mapping of prostate carcinoma foci *Cancer* **89** 1800–9
[47] Erbersdobler A, Huhle S, Palisaar J, Graefen M, Hammerer P, Noldus J and Huland H 2002 Pathological and clinical characteristics of large prostate cancers predominantly located in the transition zone *Prostate Cancer Prostatic Dis.* **5** 279–84
[48] Tao R, Tavakoli M, Sloboda R and Usmani N 2015 A comparison of US-versus MR-based 3D prostate shapes using radial basis function interpolation and statistical shape models *IEEE J. Biomed. Health Inform.* **19** 623–34
[49] Dinh H Q, Turk G and Slabaugh G 2002 Reconstructing surfaces by volumetric regularization using radial basis functions *IEEE Trans. Pattern Anal. Mach. Intell.* **24** 1358–71
[50] Frimmel H, Egevad L, Bengtsson E and Busch C 1999 Modeling prostate cancer distributions *Urology* **54** 1028–34
[51] Kim K H, Lim S K, Shin T-Y, Kang D R, Han W K, Chung B H, Rha K H and Hong S J 2013 Tumor volume adds prognostic value in patients with organ-confined prostate cancer *Ann. Surg. Oncol.* **20** 3133–9